Electronic Supplementary Material (ESI) for Chemical Science.

Supplementary Information

Identifying the Molecular Adsorption Site of a Single Molecule Junction Through Combined Raman and Conductance Studies

S. Kaneko[†], E. Montes[‡], S. Suzuki[†], S. Fujii[†], T. Nishino[†], K. Tsukagoshi[§], K. Ikeda[|], H. Kano[⊥], H. Nakamura[#]*, H. Vázquez[‡]*, M. Kiguchi[†]*

*Corresponding authors E-mail: kiguti@chem.titech.ac.jp, (M.K.) vazquez@fzu.cz, (H.V.),
hs-nakamura@aist.go.jp. (H.N.)

[†]Department of Chemistry, School of Science, Tokyo Institute of Technology, 2-12-1 W4-10 Ookayama, Meguro-ku, Tokyo 152-8551, Japan
[‡]Institute of Physics, Academy of Sciences of the Czech Republic, Cukrovarnicka 10, Prague CZ-162 00, Czech Republic
[§]International Center for Materials Nanoarchitectonics (WPI-MANA), National Institute for Materials Science (NIMS), Tsukuba, Ibaraki 305-0044, Japan
[|]Graduate School of Engineering, Nagoya Institute of Technology, Gokiso, Showa, Nagoya 466-8555, Japan
[⊥]Institute of Applied Physics, University of Tsukuba Tennodai 1-1-1, Tsukuba, Ibaraki 305-8573, Japan
[#]CD-FMat, National Institute of Advanced Industrial Science and Technology (AIST), Central 2, Umezono 1-1-1, Tsukuba, Ibaraki, 305-8568, Japan

Table of Contents

S1. Experimental details.

The nano-fabricated MCBJ substrate was mounted on a three-point bending mechanism, consisting of a stacked piezo-element (NEC tokin) and two fixed counter supports (Figure S1). Molecular junctions were prepared by depositing a drop of a 1mM ABT or BDT ethanol solution onto the unbroken Au electrode allowing molecular self-assembly on the Au surface. The sample was dried in ambient air (~15 minutes). For the simultaneous surface-enhanced Raman spectroscopy (SERS) and electrical measurements a self-breaking process was employed. We prepared the Au atomic junction having a conductance of 3 G_0 by controlling the separation of the electrodes. The push-rod was hold in position, and the electrical and Raman signals were constantly monitored while the metallic contact was allowed to break spontaneously from thermal fluctuations and current-induced forces. This immobile substrate methodology is especially appropriate to perform reliable SERS measurements. After the breaking, we made the metal contact by controlling the separation of the electrodes. Here, the conductance was larger than 3 G_0. And, we then prepared the Au atomic junction having a conductance of 3 G_0 by controlling the separation of the electrodes, and started the measurements again. The number of samples are 4 (bias voltage=0V), 7 (0.1V), 4 (0.2V) for ABT junction, 2 (0V), 10 (0.1 V), 3 (0.2 V) for BDT junction. In this experiment, we define the single molecule junctions as ones having conductance between 0.05 G_0 and 1×10^{-4} G_0 based on the previously reported studies.

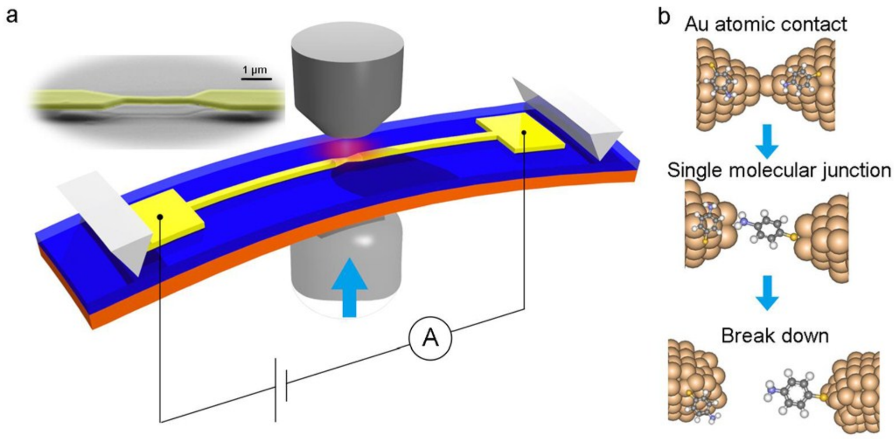

Figure S1. Schematic of MCBJ setup. (**a**) Schematic of measurement setup used in this work together with the SEM image of the electrodes. Raman spectra were detected using a Raman microprobe spectrometer while simultaneous electrical measurements were performed using a programmable pico-ammeter. (**b**) Formation process of the single molecule junction.

S2. Spatial distribution of SERS signal.

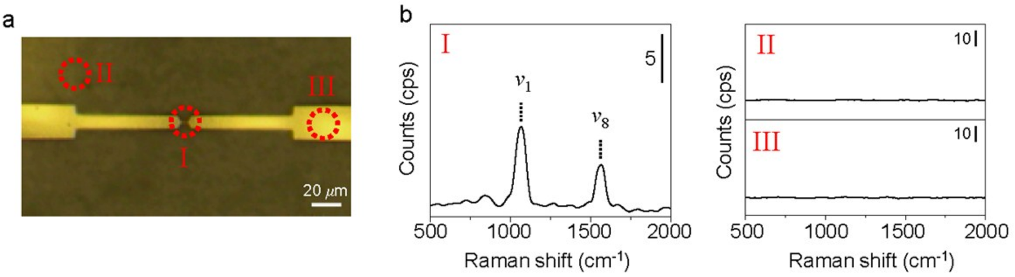

Figure S2. Spatial distribution of SERS signal. (**a**) Optical microscope image of the MCBJ substrate showing the Au nano electrode. (**b**) SERS spectra collected from the nano-gap between Au electrodes (I), the surrounding SiO_2 layer (II), and the flat area of the Au electrodes (III).

S3. Correlation between SERS intensity and conductance.

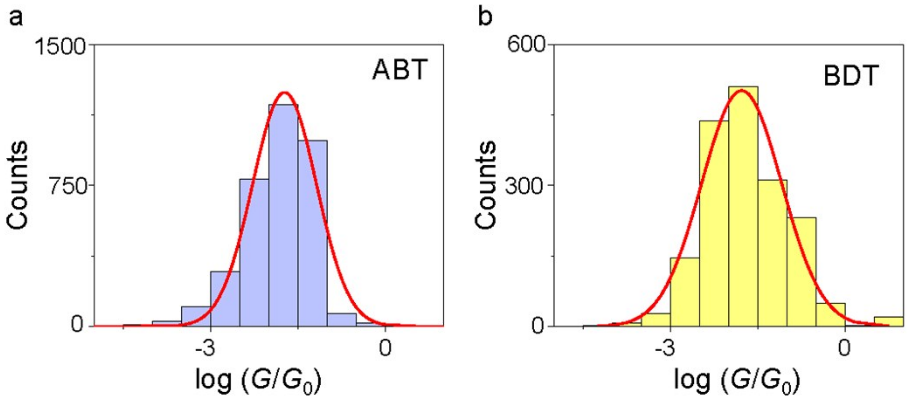

Figure S3. Conductance histogram of ABT and BDT molecular junctions. Conductance histogram of the (**a**) ABT and (**b**) BDT molecule junctions constructed from 3792 (ABT) and 2038 (BDT) molecule junctions, where the intensity of v_{8a} mode is more than 10 cps. The solid line represents the curve fitting using Gaussian. The conductance is determined by the average conductance value in the regime from 0.01V to 0.1V of *I-V* curve.

S4. Simultaneous SERS and *I-V* measurements.

Simultaneous SERS and *I-V* measurement are performed during the self-breaking process of the junction. Initially, conductance values greater than the fundamental quantum of conductance ($G_0 = 2e^2/h$) are observed for the unbroken Au contact (Figure S4, I). Conductance values of 1 G_0 indicate the formation of an atomic Au contact. At this stage, the SERS spectra features a number of weak background signals, and the *I-V* curves exhibit a steep linear response characteristic of a metallic contact (I). Conductance drops to approximately 10^{-2} G_0, which is in good agreement with the previously reported conductance values of a BDT or ABT single molecule junction, indicating the presence of a single molecule suspended across the electrode nano-gap. Here, a marked enhancement of the SERS intensity and the nonlinear *I-V* curve characteristic of molecular charge transport are registered (II). Finally, rupture of the molecular junction leads to a second conductance drop (< 10^{-4} G_0) accompanied by a loss of the marked SERS enhancement and a flat *I-V* curve (III).

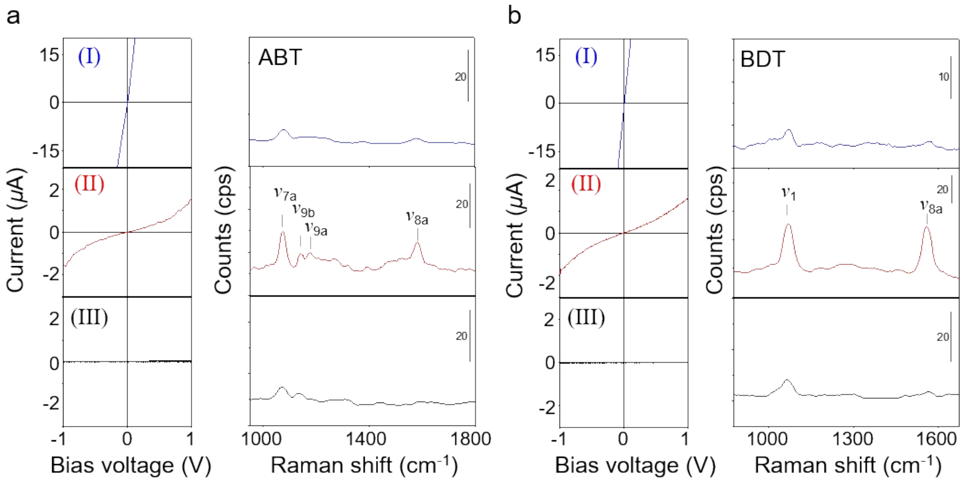

Figure S4. Simultaneous SERS and *I-V* measurement. Examples of simultaneous *I-V* and SERS measurements upon rupture of the Au contact covered with (**a**) ABT and (**b**) BDT. The ring breathing (v_1) and C-C bond stretching (v_{8a}) vibrational modes are observed for BDT, while the C-S stretching mode (v_{7a}), C-H bending (v_{9b}, v_{9a}) and C-C bond stretching (v_{8a}) vibrational modes are observed for ABT single molecule junction. The conductance of the ABT and BDT single-molecule junction is 0.01 G_0 at region (II). The bias voltage is 0.1 V during the SERS measurement.

S5. Time evolution of SERS spectra for single-molecule junction using high concentration ABT solution.

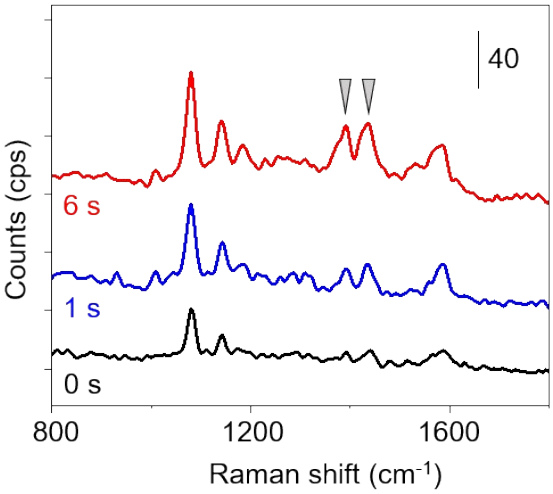

Figure S5. Time evolution of SERS spectra for ABT single-molecule junction, when we use 5mM ABT ethanol solution**.** The bias voltage is 0.1 V during the SERS measurement. The marked 1380cm^{-1} and 1430cm^{-1} peaks correspond to the ABT dimer.

S6. Analysis of *I-V* curves.

We analyses the measured *I-V* curves based on a single level tunneling model.[1] In this model, the transmission probability as a function of incident energy $\tau(E)$ is represented given by

$$\tau(E) = \frac{\Gamma^2}{\Gamma^2 + (E-\varepsilon)^2} \tag{S1}$$

where ε is the energy of the relevant conducting orbital (which DFT calculations set as the HOMO, see below), and Γ is the electronic coupling between the molecule and the metal electrode. Integration of the transmission probability within an energy window given by the chemical potentials of the electrodes results in an analytical expression for the *I-V* curve of the single molecule junction given by

$$I(V) = \frac{2e}{h}\Gamma\left\{\tan^{-1}\left(\frac{eV - 2\varepsilon}{2\Gamma}\right) + \tan^{-1}\left(\frac{eV + 2\varepsilon}{2\Gamma}\right)\right\} \tag{S2}$$

The Γ is obtained by fitting the measured *I-V* curve to equation (S2).

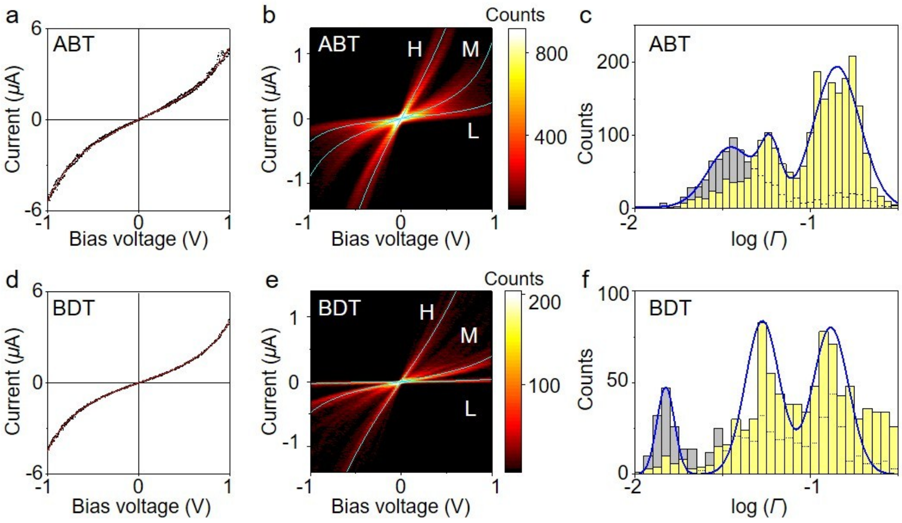

Figure S6. *I-V* measurement of ABT and BDT molecular junctions. (**a, d**) Typical *I-V* curves observed for (**a**) ABT and (**d**) BDT single molecule junctions with a conductance value of 0.026 G_0 for BDT and 0.036 G_0 for ABT around 0 bias regime (-0.1V~0.1 V). The overlaid red lines show the single level tunneling fitting. The fitting parameters are $\varepsilon = 0.72$ eV, $\Gamma = 0.14$ eV for ABT, $\varepsilon = 0.67$ eV, $\Gamma = 0.11$ eV for BDT. (**b, e**) Bi-dimensional *I-V* histogram of (**b**) ABT and (**e**) BDT single molecule junctions. The three most probable curves are fitted to a single-level tunneling transport model (light blue solid lines). The energy difference (ε) and coupling values (Γ) are ε=0.72 eV, Γ=0.14 eV, ε=0.67 eV, Γ=0.053 eV, ε=0.71 eV, Γ=0.031 eV for the high (H: conductance (G=0.032 G_0), medium (M: G=4.9×10^{-3} G_0), and low (L: G= 1.9×10^{-3} G_0) states, respectively for ABT, ε=0.84 eV, Γ=0.14 eV, ε=0.79 eV, Γ=0.046 eV, ε=0.76 eV, Γ=0.012 eV for the high (H: G=0.024 G_0), medium (M: G=3.4×10^{-3} G_0), and low (L: G= 3.9×10^{-4} G_0) states, respectively for BDT. Distribution of electronic coupling for (**c**) ABT and (**f**) BDT single molecule junctions, obtained from the 3572 (ABT) and 1529 (BDT) molecular junctions. The yellow counts correspond to the ν_{8a} active samples, where the intensity of ν_{8a} mode is more than 10 cps. The number of the ν_{8a} active samples are 2391 (ABT), 945 (BDT).

The site selectivity of SERS can be explained by the relationship between electronic coupling strength and SERS intensity. Figure S7 shows the correlation between the intensity of the ν_{8a} mode in SERS (I_s) and Γ on a log-log plot. The SERS intensity increases with Γ. The observed distribution clearly corresponds to a power law relationship, with $I_s \propto \Gamma^{0.17}$ and $\Gamma^{0.45}$ for ABT and BDT single molecule junction, respectively. The relationship between I_s and Γ can be explained by considering the SERS enhancement mechanism. The SERS signal is enhanced by the electromagnetic (EM) and chemical (CM) effects.[2] The strong electric field is formed between metal electrodes caused by the excitation of localized surface plasmon. The EM contribution is enormous large for SERS of single molecule junction, but its contribution does not sensitive to local atomic configuration, and it is nearly constant among the single molecule junctions. In contrast, the CM effect is ascribed to charge transfer resonance at metal-molecule interface, and thus the CM contribution depends on the metal-molecule interaction.[2] The charge transfer resonance easily occurs when the metal-molecule interaction is strong. Therefore, the CM contribution increases with the metal-molecule interaction, Γ. This scenario is supported by the previously reported theoretical calculation based on the single level Anderson model by using a time-dependent non-equilibrium Green's function (NEGF) approach. [3] In this study, we define that the SERS active sample is one where the intensity of SERS signal is more than 10cps (threshold count). The SERS signal from the L state would not be effectively enhanced due to the weak metal-molecule interaction, and thus its intensity is under the threshold count.

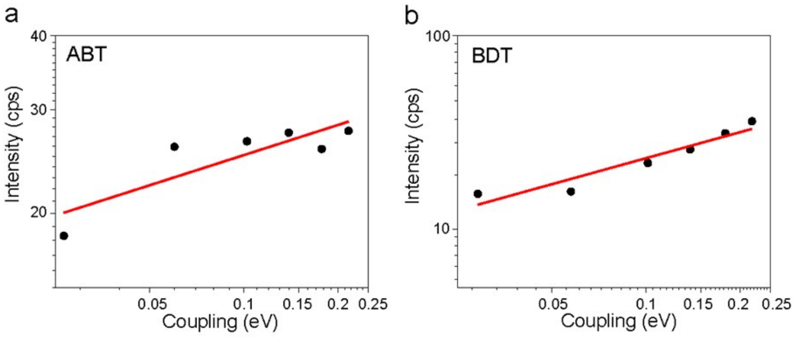

Figure S7. Correlation between the average intensity of the SERS signal. The average intensity of the SERS signal for (**a**) ABT and (**b**) BDT single molecule junction as a function of Γ on a log-log plot obtained from 3792 (ABT) and 2038(BDT) molecular junctions where the intensity of ν_{8a} mode is more than 10 cps.

S7. Definition of multiple conductance states based on the combination analysis of SERS and *I-V* measurements.

Figure S8 shows the examples of SERS of BDT single molecule junctions during the sequential measurement (10 spectra), where the sample condition does not change. The peak position is determined by the fitting the experimental data with the Lorentz function (red curve). The peak position does not change with the sample within 0.8 cm^{-1}. So, we define the Raman shift as the peak position of each SERS spectrum.

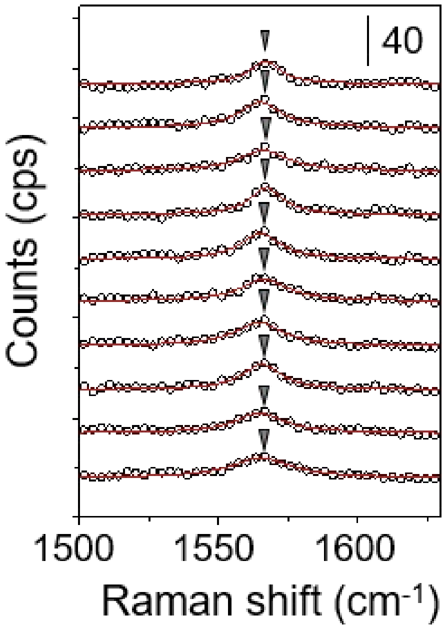

Figure. S8. SERS of BDT single molecule junction of ten samples. The bias voltage is 0.1V and the integration time is 1sec. The red curve is the fitted one with Lorentz function.

The H and M regions and the boundary are defined using the two dimensional electronic coupling (Γ)-Raman shift (ν) histogram. We explain this process using the results of the ABT single molecule junction (Figure S9) The H and M regions are defined as the areas surrounded by dotted lines where the count is larger than the threshold value. The threshold value is defined as the 80% of maximum count of the H and M regions. The boundary line (white line) is defined by the following processes. First, we evaluate the maximum Raman shift of the H state ($\nu_{\mathrm{max;H}}$) and minimum Raman shift of the M state ($\nu_{\mathrm{min;M}}$). At the Raman shift of $\nu_{\mathrm{max;H}}$ (vertical dotted line), we obtain the average value of the maxim value of the coupling for the M state and coupling of the H state. At the point $M_{max;int}$, the coupling is this averaged value and Raman shift is $\nu_{max;H}$. In a similar manner, we define point $M_{min;int}$. The boundary line is one connected the points of $M_{min;int}$ and $M_{max;int}$..

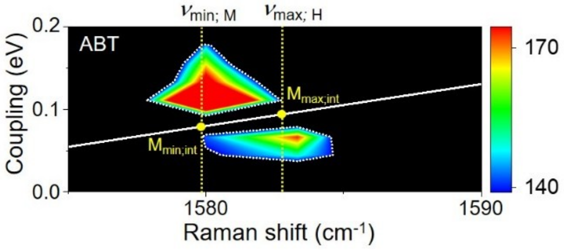

Figure S9. Two dimensional electronic coupling-Raman shift histogram. Two dimensional electronic coupling (Γ)-Raman shift (ν) histogram of ABT single molecule junction constructed from 3792 (ABT) samples using a bin size of 0.02 eV and 3 cm^{-1}. The bias voltage is 0.1V. The white dotted line represents the boundary of the bridge and hollow regions. The yellow dotted line represents the boundary of the two states.

S8. DFT calculations of conductance states.

Figure S10 shows the three different configurations considered for BDT. They consist of one, two or three Au atoms, resulting in atop, bridge or hollow structures, respectively. The same kind of bonding configuration is adopted for both metal-molecule interfaces. For both ABT and BDT, the junctions are relaxed. First, the vertical electrode separation distance is optimized. Then, in a unit cell consisting of five Au layers (each with 16 atoms per layer) and using a Monkhorst-Pack k-point mesh of 2×2×1 density, the geometry is optimized until the Hellmann-Feynman forces acting on all molecular and tip atoms is below 0.02 eV/Å. [4]

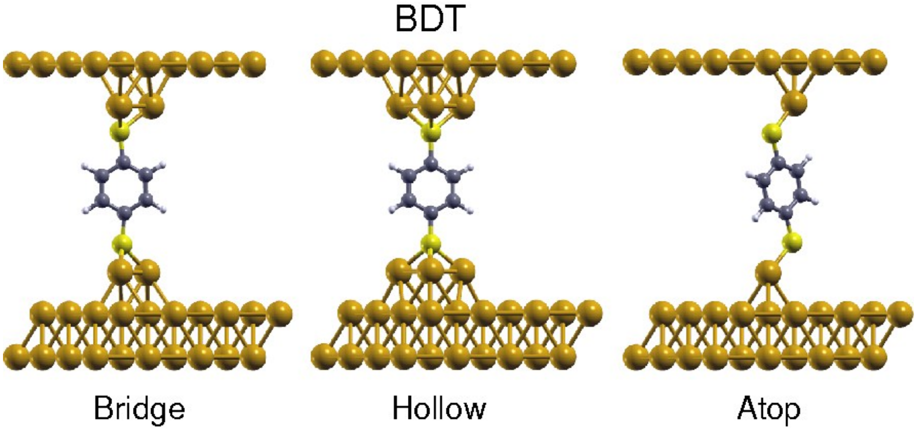

Figure S10. Optimized structures for BDT. Different binding configurations, bridge, hollow and atop.

Conductance is calculated at optimized geometries using the Non-Equilibrium Green's Function formalism.[5] Unit cells for transport calculations contain twelve Au layers. Transmission spectra for ABT and BDT in the binding configurations considered are presented in Figure S11 and S12. Top panels show DFT-based results, while bottom panels describe the corrections to DFT position of frontier levels (occupied state). In the top panels, solid lines correspond to the calculated DFT transmission spectra, while dotted lines represent a Lorentzian fitted to the conducting state (HOMO). From this fit we obtain the full width at half maximum (Γ) reported in Table S1. The bottom panels of Figure S11 and S12 show how the position of the HOMO peak given by DFT is corrected. The net energy shift ΔE is the sum of two contributions,

$$\Delta E = \Delta E_1 - \Delta E_2 \qquad \text{(S3)},$$

ΔE_1 is the self-energy correction to the level position of the isolated molecule, calculated from the total energy difference of the neutral and charged molecule

$$\Delta E_1 = E[N-1] - E[N] - \varepsilon_{DFT} \qquad \text{(S4)},$$

where E[N] is the total energy of the system, E[N-1] is the total energy of the system when an electron has been removed from the HOMO state and ε_{DFT} is the HOMO energy of the neutral system. ΔE_2 is the contribution from screening or polarization due to the metal surfaces, approximated using a classical image charge model [6-8] for the electron distribution of the HOMO

$$\Delta E_2 = \sum_n \frac{|c_n|^2}{4(Z_n - Z_{top})} + \sum_n \frac{|c_n|^2}{4(Z_n - Z_{bottom})} \qquad \text{(S5)},$$

where n is the atomic index, c_n are the coefficients of the HOMO wave function on the local-orbital basis, and $Z_n - Z_{top}$ ($Z_n - Z_{bottom}$) is the difference in z components between each molecular atom and the top (bottom) electrode. ΔE_1 shifts molecular states away from the Fermi energy, while ΔE_2 acts in the opposite direction.[6-8] The calculated net energy shifts (ΔE) for each structure (ABT or BDT) are given in Table S1. For each molecular resonance, the magnitude of the correction is completely defined by the junction structure through its electronic properties (E[N], E[N-1] and HOMO eigenstate) and geometry (image-charge screening).

Table S1. Calculated net shifts (ΔE) of the occupied resonance. Energy shift for the energy level correction of the DFT HOMO.

		ΔE (eV)
ABT	Bridge	1.15
	Hollow	1.17
	Atop	1.29
BDT	Bridge	1.08
	Hollow	1.08
	Atop	1.17

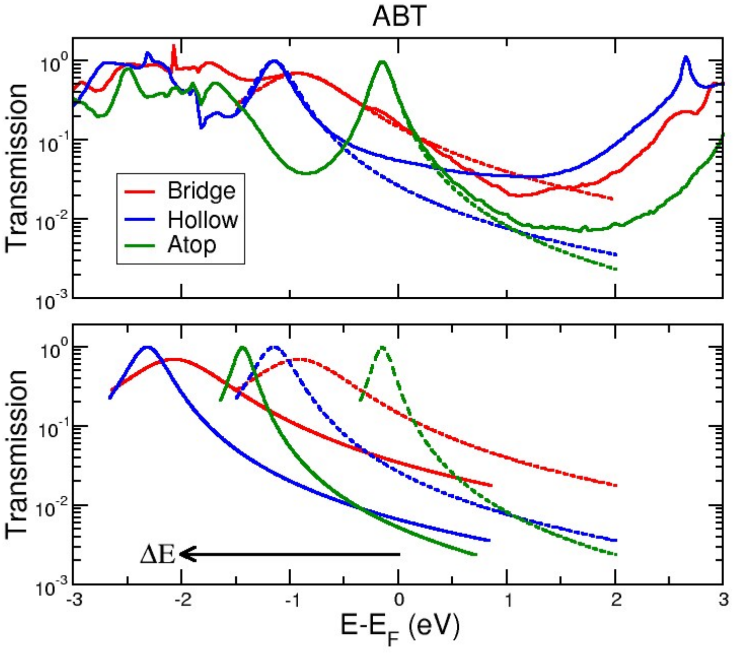

Figure S11. DFT-NEGF transmission spectra of ABT. (Top panel) DFT-NEGF transmission spectra of

ABT in the bridge, hollow and atop configurations. Dotted lines correspond to Lorentzians fitted to the conducting (HOMO) state. (Bottom panel) HOMO resonance before and after corrections to level positions.

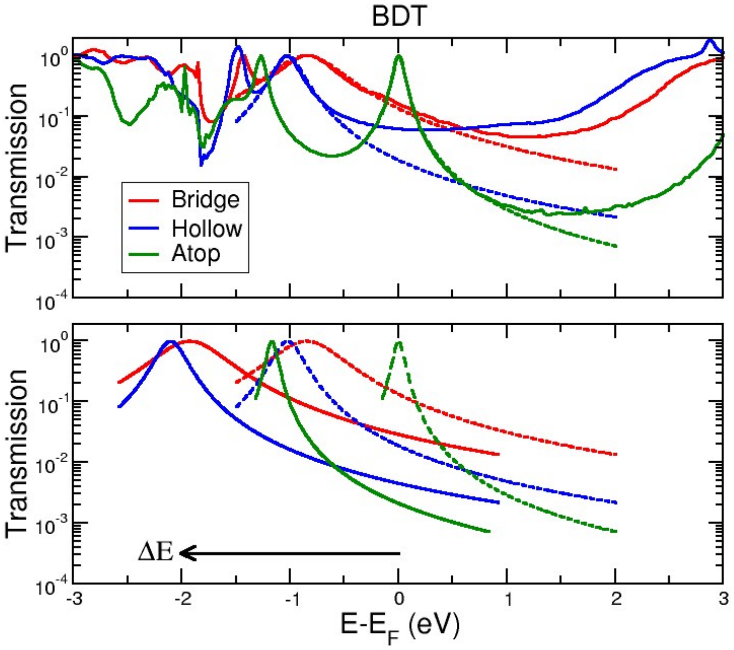

Figure S12. DFT-NEGF transmission spectra of BDT. (Top panel) DFT-NEGF transmission spectra of BDT in the bridge, hollow and atop configurations. Dotted lines correspond to Lorentzians fitted to the conducting (HOMO) state. (Bottom panel) HOMO resonance before and after corrections to level positions.

The real-space representations of the scattering states at the Fermi energy, responsible for low-bias transmission are presented in Figure 3b and Figure S13, for ABT and BDT, respectively. The nodal pattern of the scattering states resembles that of the HOMO of the isolated molecule, as shown in Figure S14.

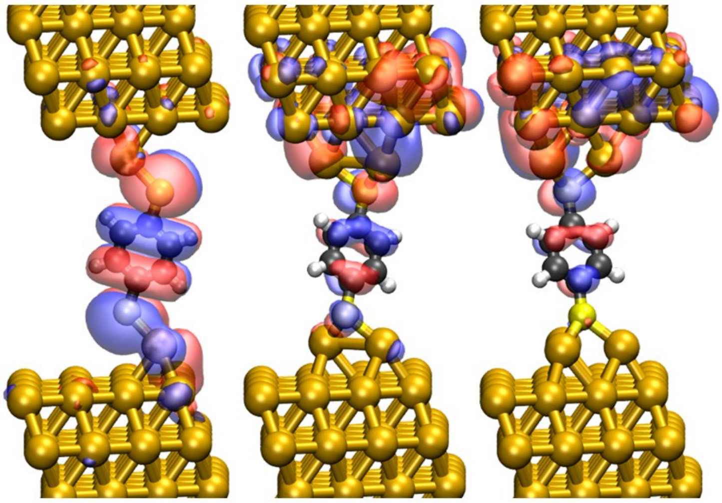

Figure S13. Transmission eigenchannels of BDT. Transmission eigenchannels of BDT at the Fermi energy for atop (left), bridge (center) and hollow (right) bonding sites.

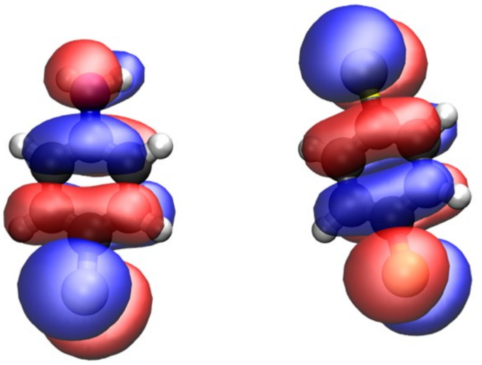

Figure S14. Isosurface plots of the molecular orbitals. Isosurface plots of the HOMO of the isolated ABT (left) and BDT (right) molecules.

DFT calculations of the vibrational energy[4] of ABT and BDT are performed on junctions having three Au layers using a denser a 5×5×1 k-point Monkhorst-Pack grid. The force constant matrix describes the movement of molecular and Au tip atoms. We unambiguously identify the energy of the C-C stretching mode (ν_{8a}), shown in Figure 3 for ABT and in Figure S10 for BDT.

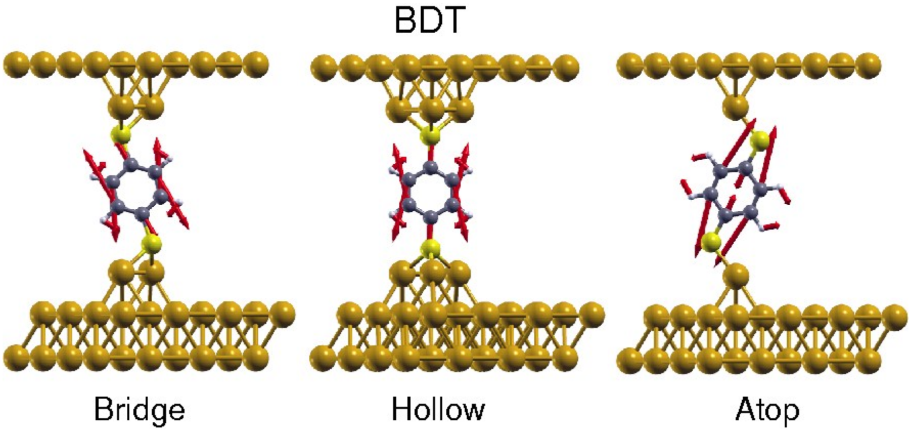

Figure S15. C-C stretching mode (ν_{8a}) for the three different binding configurations of BDT.

The amine linker is known to bind selectively to under-coordinated Au atoms. Here we have modeled it using a trimer tip. However, we have confirmed that other under-coordinated configurations induce only small changes conductance (Fig. S16). The calculated spectra are similar and changes in conductance between structures are approximately 6%. Thus we conclude that the nature of the amine contact does not strongly affect conductance.

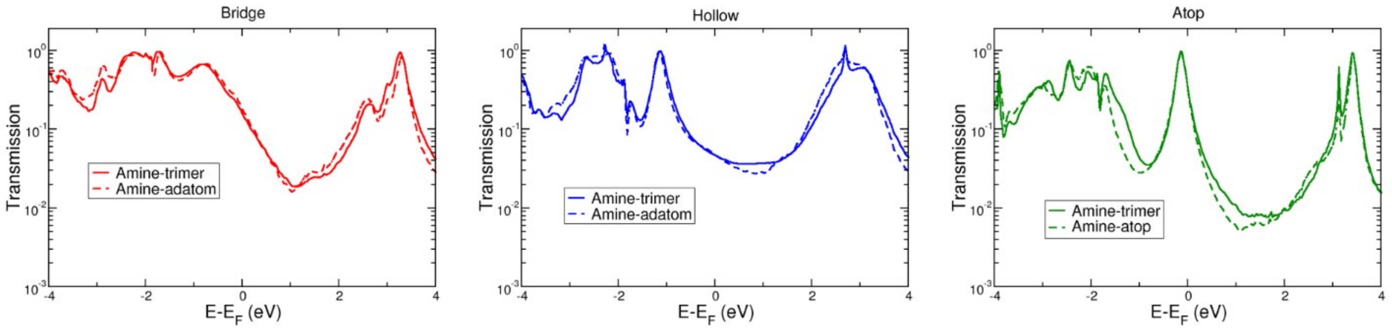

Figure S16. DFT-based transmission spectra of ABT for different tip structures on the amine contact (trimer, adatom) for a given binding site (bridge, hollow, or atop site) on the S-Au bond.

The Au-S contact, is well known for having several possible configurations. We considered the different bonding combinations between bridge, hollow and atop sites. We proceed as described before and use the one-level model to obtain the transmission spectra centered at HOMO and I-V curves for all possible configurations, shown in Figs. S17 and S18.

From these results we see that the conductance of Bridge-Bridge, Bridge-Hollow, Hollow-Adatom, Hollow-Hollow, Bridge-Adatom, Adatom-Adatom structures decreases in that order. From Fig. S6e, we can see significant I-V distributions between H and M states, and between M and L states. This spread in measured I-V curves is consistent with the range of intermediate conductance values found in our calculations.

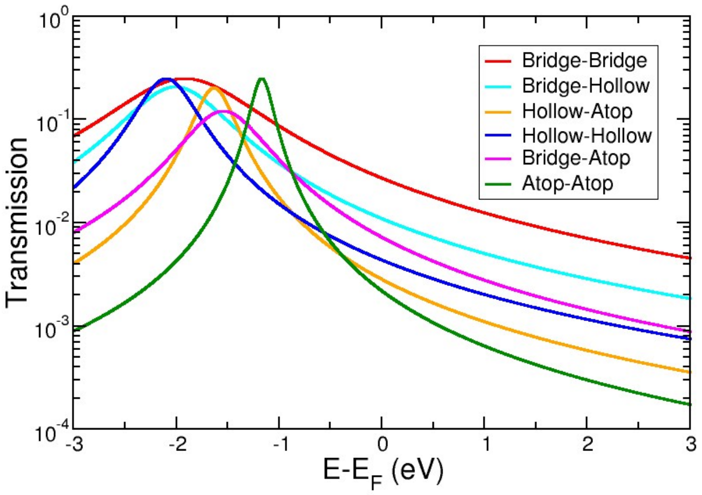

Figure S17. Transmission spectra for all possible configurations of BDT fitted with the one-level model.

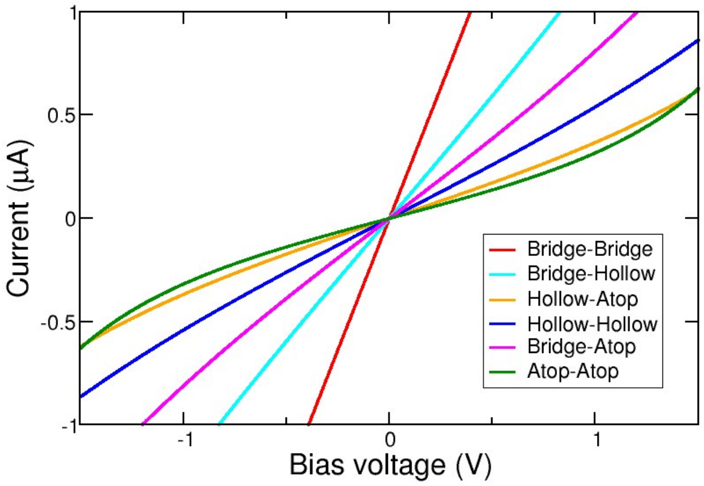

Figure S18. I-V curves for all possible configurations of BDT fitted with the one-level model.

Table S2. Comparison of measured and calculated conductance for BDT in all possible configurations. Numbers in parentheses are scaled to the value of Bridge-Bridge (high conductance) state.

			G (G_0)	
		Assignment	exp	calc
BDT	High	Bridge-Bridge	2.4×10^{-2} (1)	2.9×10^{-2} (1)
		Bridge-Hollow		1.2×10^{-2} (0.41)
		Hollow-Atop		7.7×10^{-3} (0.27)
	Medium	Hollow-Hollow	3.4×10^{-3} (0.14)	4.5×10^{-3} (0.16)
		Bridge-Atop		3.0×10^{-3} (0.10)
	Low	Atop-Atop	3.9×10^{-4} (0.02)	2.1×10^{-3} (0.07)

Table S3. Comparison of measured and calculated conducting and optical properties of the junction. Conductance (*G*), electronic coupling (*Γ*) and Raman shift (ν: ν_{8a} mode) for ABT and BDT single-molecule junctions. The *G*, *Γ,* and ν values in the parentheses are scaled by the values for the bridge (high conductance) states.

		G (G_0)			*Γ* (eV)		Vib ($\mathrm{cm^{-1}}$)	
		exp	calc	Assignment	exp	calc	exp	calc
ABT	High	3.2×10^{-2} (1)	3.5×10^{-2} (1)	Bridge	0.14 (1)	0.95 (1)	1580 (1)	1604 (1)
	Medium	4.9×10^{-3} (0.15)	6.6×10^{-3} (0.19)	Hollow	0.064 (0.46)	0.38 (0.38)	1582 (1.0013)	1607 (1.0019)
	Low	1.9×10^{-3} (0.06)	5.2×10^{-3} (0.15)	Atop	0.031 (0.22)	0.21 (0.22)		
BDT	High	2.4×10^{-2} (1)	2.9×10^{-2} (1)	Bridge	0.12 (1)	0.67 (1)	1567 (1)	1572 (1)
	Medium	3.4×10^{-3} (0.14)	4.5×10^{-3} (0.16)	Hollow	0.06 (0.52)	0.28 (0.42)	1560 (0.996)	1561 (0.993)
	Low	3.9×10^{-4} (0.02)	2.1×10^{-3} (0.07)	Atop	0.01 (0.10)	0.11 (0.16)		

S9. Time course of SERS and conductance.

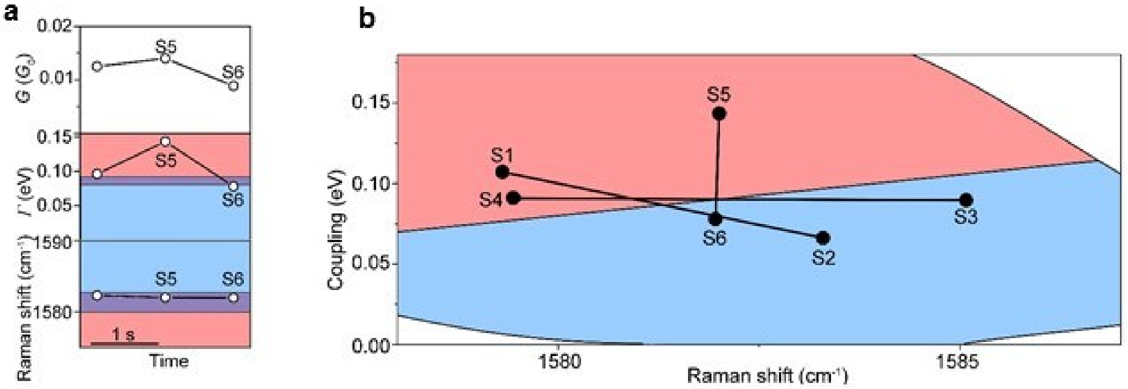

Figure S19. Transition between bridge and hollow for ABT. (a) Transition between bridge and hollow for ABT measured at bias voltage of 0.1V. The G, Γ and ν are 0.013 G_0, 0.096 eV, 1582 cm^{-1} for S5, 0.0089 G_0, 0.078 eV, 1582 cm^{-1} for S6. (b) 2D Γ-ν mapping.

S10. Effect of application of bias voltage on molecular adsorption site

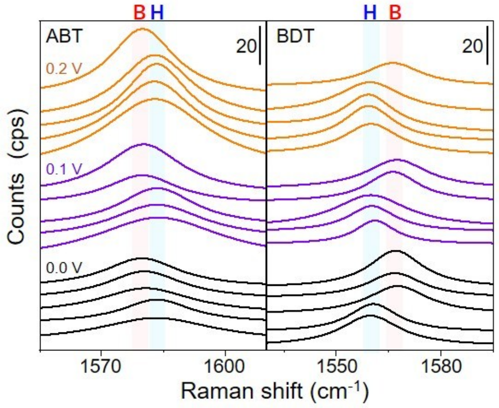

Figure S20. Examples of SERS for ABT and BDT single molecule junctions at different bias voltages.

Table S4. Distribution of molecular adsorption sites for BDT and ABT single molecule junctions determined by the combination analysis of SERS and *I-V* measurements.

		0.0 V	**0.1 V**	**0.2 V**
ABT	**Hollow (%)**	30	39	90
	Bridge (%)	70	61	10
BDT	**Hollow (%)**	39	69	89
	Bridge (%)	61	31	11

We derive the Eq. (2) in the manuscript then evaluate the required parameter set to quantify the applied bias dependency of the site population (for bridge and hollow configurations). First, we introduce the effective temperature T^{eff} to incorporate the local heating effect. According to the theoretical analysis by Todorov *et al*, the local temperature is roughly evaluated as [13]

$$T^{eff} = (T_0^4 + \gamma^4 V^2)^{1/4} \tag{S6}$$

The additional temperature term, i.e., $T^{eff}-T_0$, may be much smaller than the background temperature T_0 when the bias V is sufficiently small. Then T^{eff} may be represented as

$$T^{eff} = T_0 + \frac{\gamma^4}{4T_0^3}V^2 \tag{S7}$$

where γ depends on the system. Theoretically, it is known that γ is proportional to the electric conductance.[13] Furthermore, the threshold voltage V_c is usually introduced phenomenologically, where local heating effect is negligible in the lower bias regime than V_c.[14] Next, we incorporate the effect of current-induced force. The work done by the current-induced force suppresses the barrier height of the site transition.[15,16] Since The current induced-force consists of the electric-field force and wind force by the electric current,[15,17] the barrier suppression is roughly proportional to the magnitude of the applied bias.[18] Then the activation energy is modified as

$$E_{eff}^* = E^* - \alpha V \tag{S8}$$

where the magnitude of α depends on the local current intensity at the rupture (or reactive) point of the junction.[15,19] By inserting Eqs (S7) and (S8) into Eq. (1), we arrive Eq. (2).

In the case of the BDT junction, most of the required parameters are found in the literature as given in Table S5. Here we adopted the values given in Refs[20,21] as the parameters of the bridge BDT junction, which is termed as BDT(B) and the activation energy assumed to be equal to the energy to break Au-S bond in the junction, i.e., E^*_B is set to 0.8 eV. The parameters α_H and γ_H is estimated as 10 % of α_B and γ_B, respectively since the conductance of the hollow site, termed as BDT(H), is about 10 % of that of BDT(B) as given in Table 1 in the manuscript. It is reasonable to take the same threshold voltage to activate local heating with BDT(B) and BDT(H), and hence, we adopted the value $V_c = 0.5$ V from Refs.[20,21]

Next, we evaluate the parameters of the ABT junction. We set the activation energy of E^*_B to 0.35 eV from ref.[21] By comparing the electric conductance of ABT(B) and BDT(B) in Table S3, γ_B of ABT may be taken as 595 $KV^{1/2}$. Since the conductance of BDT(B) and ABT(B) is close, one attempts to set α_B of ABT equal to that of BDT. However, such speculation will overestimate the value because of the asymmetric contacts of the ABT junction, i.e., Au-S and Au-NH_2 have potentially different electronic coupling strength. According to analysis of the conductive HOMO in Figure S14, the electronic density at -NH_2 is about 1/3 of the density in the -S region. As a result, the local electric current at -NH_2 site can roughly 1/3 of the intensity on -S, i.e., α_B of ABT may be taken as 1/3 of the value of BDT. The parameters of ABT(H) are determined by the similar procedure used to obtain those of BDT(H). All of the parameters are summarized in Table S5.

Table S5. The parameter set used to analyze bias-dependence of site population.[a]

	V_c (V)	E^*_B (eV)	E^*_H (eV)	γ_B (KV$^{1/2}$)	γ_H	α_B (eV/V)	α_H
BDT	0.50	0.80	0.78	446	44.6	0.30	0.03
ABT	0.00	0.35	0.34	595	59.5	0.10	0.01

[a]The values shared in the grey are taken from Refs [20,21]

References

1. Y. Komoto, Y. Isshiki, S. Fujii, T. Nishino and M. Kiguchi, *Chem. Asian J.*, 2017, **12**, 440-445.
2. J. R. Lombardi, R. L. Birke, T. Lu and J. Xu, *J. Chem. Phys.*, 1986, **84**, 4174-4180.
3. H. J. W. Haug and A.-P. Jauho, *Quantum Kinetics in Transport and Optics of Semiconductors*, Springer, Berlin, 2nd edn., 2007.
4. J. M. Soler, E. Artacho, J. D. Gale, A. Garcia, J. Junquera, P. Ordejon and D. Sanchez-Portal, *J. Phys. Condens. Matter*, 2002, **14**, 2745-2779.
5. M. Brandbyge, J. L. Mozos, P. Ordejon, J. Taylor and K. Stokbro, *Phys. Rev. B*, 2002, **65**, 165401.
6. J. B. Neaton, M. S. Hybertsen and S. G. Louie, *Phys. Rev. Lett.*, 2006, **97**, 216405.
7. S. Y. Quek, L. Venkataraman, H. J. Choi, S. G. Louie, M. S. Hybertsen and J. B. Neaton, *Nano Lett.*, 2007, **7**, 3477-3482.
8. F. Flores, J. Ortega and H. Vazquez, *Phys. Chem. Chem. Phys.*, 2009, **11**, 8658-8675.
9. L. A. Zotti, T. Kirchner, J. C. Cuevas, F. Pauly, T. Huhn, E. Scheer and A. Erbe, *Small*, 2010, **6**, 1529-1535.
10. Z. Li and D. S. Kosov, *Phys. Rev. B*, 2007, **76**, 035415.
11. L. Venkataraman, J. E. Klare, I. W. Tam, C. Nuckolls, M. S. Hybertsen and M. L. Steigerwald, *Nano Lett.*, 2006, **6**, 458-462.
12. Y. Komoto, S. Fujii, H. Nakamura, T. Tada, T. Nishino and M. Kiguchi, *Sci. Rep.*, 2016, **6**, 26606.
13. T. N. Todorov, *Philos. Mag. B*, 1998, **77**, 965-973.
14. Y.-C. Chen, M. Zwolak and M. Di Ventra, *Nano Lett.*, 2003, **3**, 1691-1694.
15. R. X. Zhang, I. Rungger, S. Sanvito and S. M. Hou, *Phys. Rev. B*, 2011, **84**, 085445.
16. T. Ohto, I. Rungger, K. Yamashita, H. Nakamura and S. Sanvito, *Phys. Rev. B*, 2013, **87**, 205439.
17. T. N. Todorov, J. Hoekstra and A. P. Sutton, *Philos. Mag. B*, 2000, **80**, 421-455.
18. M. Di Ventra, *Electrical Transport in Nanoscale Systems*, Cambridge Univ. Press, Cambridge, 2008.
19. H. Nakamura, *J. Phys. Chem. C*, 2010, **114**, 12280-12289.
20. M. Tsutsui, M. Taniguchi and T. Kawai, *Nano Lett.*, 2008, **8**, 3293-3297.
21. M. Tsutsui, M. Taniguchi and T. Kawai, *J. Am. Chem. Soc.*, 2009, **131**, 10552-10556.